

Elaborating Higgs to dimuon decay from gluon fusion by decorrelation and jet substructure

Subin Han¹ and Hyung Do Kim¹

¹*Department of Physics and Astronomy and Center for Theoretical Physics,
Seoul National University, Seoul, Korea 08826*

Abstract

Discovery of the Higgs boson decay to dimuon is anticipated soon based on the current evidence. Precise categorization of the events without affecting the invariant mass shape is crucial in the analysis. Decorrelation of the invariant mass and the output of discriminators (the score of discriminators) is essential for consistent and precise analysis. In this paper we use distance correlation as the additional loss function to achieve the decorrelation for discriminators and examine various analysis methods. The analyses with and without jet substructure variables are presented. Adding jet substructure variables considerably improves the significance of the Higgs to dimuon signal from gluon fusion.

I. INTRODUCTION

After Higgs discovery [1][2], various properties of Higgs have been measured including Higgs couplings to Standard Model (SM) particles. The SM predicts the Higgs coupling to a particle is proportional to its mass. Accordingly, Higgs couplings to heavy particles, such as gauge bosons and third generation fermions, are well measured [3][4][5][6]. However, couplings to relatively light particles have not been satisfactorily measured so far. The Higgs to dimuon channel is the most sensitive channel among the second generation fermions at the LHC due to the relatively clean leptonic final states. The property of Higgs couplings to light fermions can verify the Higgs mechanism of the SM more accurately. Furthermore, the growing interest towards a muon collider makes this channel more interesting.

In 2020, the decay of Higgs to dimuon was barely confirmed to be consistent with the SM [7]. The observed (expected) significance was 3.0σ (2.5σ). The analysis was performed separately for each Higgs production channel. However, the signal-to-background ratio for each channel was not sufficient to extract the number of signal events ($\sim 0.3\%$ for ggH channel at Higgs mass). To increase the sensitivity, each channel was further divided into several categories with different signal-to-background ratios based on the output of discriminators. The dimuon invariant mass $m_{\mu\mu}$ is an excellent variable for distinguishing the resonance peak of the Higgs signal from the background events. Therefore extraction of the number of signal and background events as well as the calculation of discovery significance were conducted by fitting data to the expected $m_{\mu\mu}$ distribution. Several uncertainties arising from the simulation could be reduced through shape analysis during the distribution fitting. A crucial requirement for the analyses using categorization above is that the information about the invariant mass should not be used in the categorization process. In other words, the output of discriminators, or the discriminator score, should be

statistically independent of the invariant mass. Categorization by a score which is statistically dependent on the invariant mass generally results in different invariant mass distributions for each category, $f(m|\text{score}) \neq f(m)$, where f represents the probability density function. If the invariant mass distribution is distorted, the number of events extracted from each category can not be reliably trusted. In extreme cases, a resonance peak near the Higgs mass may appear in the background $m_{\mu\mu}$ distribution (See Fig.1 for example) adding a significant uncertainties on the number of signal events near the Higgs bump region. In addition, if we fit to the invariant mass after the categorization by a discriminator correlated to the invariant mass, it results in double usage of the invariant mass, compounding the error. Therefore the standard likelihood fitting to the invariant mass distribution can be consistently combined with machine discriminator results only when two results are decorrelated/deassociated.¹

To avoid the distortions in the invariant mass distribution that arise when events are selected by a discriminator correlated with the invariant mass, researchers have not only securely excluded the invariant mass but also carefully selected other variables to make the categories as insensitive to the invariant mass as possible. However, as will be seen in the paper, machine discriminators generally learn about $m_{\mu\mu}$ since it has strong discrimination power. An ad hoc choice of variables which seemingly unrelated to the $m_{\mu\mu}$, qualitative check of distortion in distributions after categorization [10] and a posteriori modification of fitting functions are not satisfactory solutions. In this paper we provide a quantitative and consistent framework to deal with this problem. Among the various measures of dependence between two sets of feature variables, we choose ‘distance correlation’ [9] [11] since it is differentiable, so being compatible with deep learning frameworks, well defined in both population and sample spaces, and

¹ Technically, the term ‘deassociate/deassociation’ is more appropriate [8], but we will use the term ‘decorrelate/decorrelation’ following other literature [9]

capable of capturing both linear and non-linear dependence. At the same time the range is well defined such that it is 0 when there is no correlation and is 1 when it is fully deterministic/dependent. By leveraging the flexibility of deep neural network (DNN), we use the distance correlation between $m_{\mu\mu}$ and output of discriminator as an additional loss for training the discriminator. As a result, it has been found that almost perfect statistical independence (for both signal and background data classes simultaneously) between $m_{\mu\mu}$ and the discriminator output can be systematically achieved, enabling us to choose the required degrees of independence, which is crucial for accurate analysis, despite being in a trade-off relation to the performance of the discriminator. By carefully balancing this trade-off, this approach ensures reliable categorization without compromising the integrity of the invariant mass distribution. Compared to the analysis using only the kinematic variables of reconstructed particle objects, incorporating jet substructure variables of the jets associated with the dimuon system as additional input features for the discriminator can provide extra power, especially in discriminating the gluon dominant ggH signal from other background processes. Currently the vector boson fusion (VBF) is the leading production channel for the Higgs to dimuon discovery despite the fact that the ggH production cross section is more than 10 times larger than VBF one at $\sqrt{s} = 13$ TeV [12]. In [13], it has been demonstrated that ggH channel can be exploited to improve the sensitivity of the Higgs invisible signal if jet substructure variables are fully utilized to distinguish the flavors and kinematics of ISR by DNN analysis. The difference in parton luminosities and QCD color factors of vertices results in the signal ggH ISR to be gluon-rich, while the background Drell-Yan (DY) ISR to be quark-rich. In addition, due to the helicity conservation, ggH ISR has a deficit of quark jets at the central rapidity region. ² In this study, the same method is used to improve the

² There is no issue of decorrelation in Higgs to invisible study, the treatment of systematic uncertainties originating from the simulation remain as open question.

sensitivity of Higgs to dimuon signal from ggH channel.

The paper is composed as following. In section.II, we first outline the event simulation and ggH selection cuts. We also summarize the analysis strategy including training variables, common training schemes, and the categorization procedure. In section.III, we introduce three types of discriminators and compare their result in detail. In particular, with the $m_{\mu\mu}$ decorrelated discriminator implemented using the distance correlation, the degree of statistical independence and the discrimination performance will be compared. In section. IV, we compute the discovery significance using the categorized events and check the effect of including jet substructure variables.

II. EVENTS AND ANALYSIS STRATEGY

When an event is classified being from ggH, it means that the event passed all selection cuts to identify ggH, regardless of genuine origin of the event. Therefore, all possible Higgs production channels have to be simulated. However, the contribution from other channels to the ggH signals is much smaller than genuine ggH channel due to their small cross sections. Next to leading order contribution is from VBF channel which is less than 5% of ggH channel. Thus we simulated only ggH and VBF channel. Similarly, there are many channels which act as backgrounds against ggH. Among them, we included the dominant background DY and $t\bar{t}$ which has non-negligible contribution to multi-jet process (more than 20% of DY). All the events are simulated by MadGraph5_aMC@NLO [14] at $\sqrt{s} = 13$ TeV. Each simulation was done inclusively for the number of jets, so that we can properly include both soft and hard jet emissions.

After the simulation, the selection of events for ggH was conducted. Basically, an event is required to have two oppositely charged muons with $p_T > 20$ GeV and

$|\eta| < 2.4$. Any events including b-jet and/or additional charged lepton are vetoed to avoid overlap with $t\bar{t}H$ and VH channel. Finally, events with two energetic and largely separated jets ($m_{jj} > 400$ GeV, $|\Delta\eta_{jj}| > 2.5$) are rejected as those are to be identified as VBF.

To enhance the signal-to-background ratio, various information other than $m_{\mu\mu}$ is used to divide the total data into some categories. Recently, with huge development of machine learning techniques, output of machine discriminators are frequently used as a criterion for categorization to use various variables simultaneously. The set of training variables used by the CMS collaboration is denoted by $S_{n_{\text{jet}}}$ for each number of jet n_{jet} . $S_{n_{\text{jet}}}$ are carefully selected to exclude the $m_{\mu\mu}$ information. Please note that $n_{\text{jet}} = 2$ means events with at least two jets and the kinematics of jets are included in terms of pseudo rapidity η of leading and next to leading jet. To exploit ISR characteristic of ggH channel, we also included set of jet substructure variables $JS \equiv \{n_{\text{track}}, \text{girth}, \text{broadening}, C_1^{\beta=0.2}, \text{RMS} - p_T, \text{Pull-vector}\}$ for each jet. Therefore total set of variables including jet substructure variables are $J_0 \equiv S_0$, $J_1 \equiv S_1 \cup JS_1$ and $J_2 \equiv S_2 \cup JS_1 \cup JS_2$. See Appendix A for more detail.

The discriminators are trained separately for events with different number of jets n_{jet} because we have different number of training variables for each n_{jet} . The training sample consists of one million signals and backgrounds respectively, 70% for training and 30% for validation. We will train three types of machine discriminators to compare the results; BDT as a benchmark, (ordinary) DNN and decorrelated DNN. After the training, total data set is divided into categories according to the output of discriminators, or equivalently, by the signal efficiency. The boundaries are recursively selected to maximize the total expected significance with S/\sqrt{B} as a figure of merit, while minimizing the number of categories (until the gain from additional boundary is less than 1%).

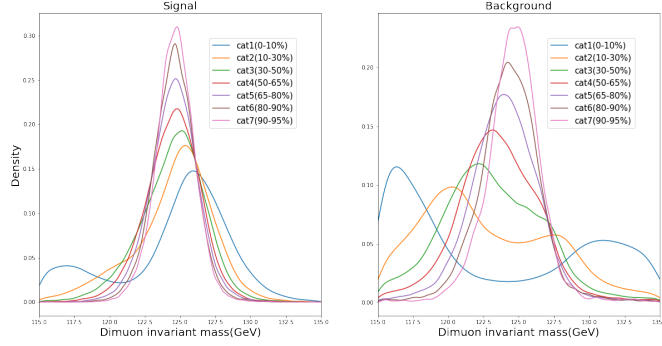
A typical next step is to extract the number of events from fitting of data to $m_{\mu\mu}$

distribution. However we will skip the extraction procedure and use the number of events by simulation directly because we do not have real observed data to fit. Since we already used large data, fitting to another set of simulated data is not worth much. Though our result depends on the simulated data, there is no significant problem in comparison between discrimination schemes and check the impact of including jet substructure variables. Therefore after the categorization, we will compute the discovery significance by profile likelihood fitting to the $m_{\mu\mu}$ distribution.

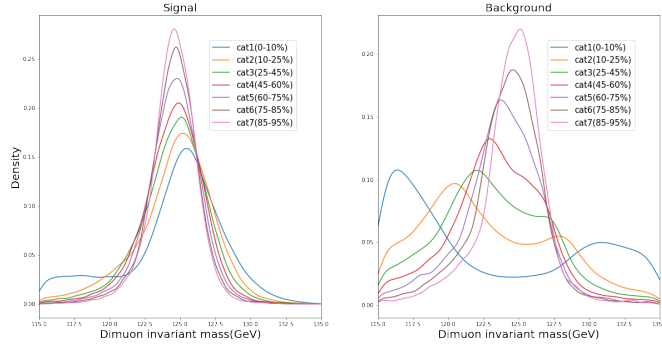
III. DISCRIMINATORS

The astonishing success of DNN is based on the ability to build a hidden representation from the training variables. However, due to the very feature, DNN generally reconstruct the invariant mass even if it is not directly included in training variables. As a result, the distributions of categorized events are largely distorted. We used **PyTorch** [15] to implement DNN and used **SCIKIT LEARN** [16] for preprocessing. Selected models are given in Appendix.B2. Fig.1 shows the actual distortion by ordinary DNN discriminator. In categories with high signal purity, even the background distribution resembles the resonance peak of the signal. It can mimic signals and overestimate the number of signal events. Therefore, the extraction of the number of events by fitting to $m_{\mu\mu}$ is not valid any more under such distortion. In such cases, it would be more appropriate to extract the number of events by fitting signal strength modifier to the distribution of output directly. However, this method suffers from large systematic uncertainties from simulation and training and therefore fitting to the invariant mass is more preferred generally.

The CMS collaboration used boosted decision tree (BDT) to categorize their ggH data. The tree-based models including BDT are essentially complex collections of cuts on training variables. Therefore, generally BDT has good performance for the-



(a) DNN; **without** jet substructure variables($S_{n_{\text{jet}}}$)



(b) DNN; **with** jet substructure variables($J_{n_{\text{jet}}}$)

FIG. 1. $m_{\mu\mu}$ distribution binned by optimal boundaries chosen by output of (ordinary) DNN discriminators.

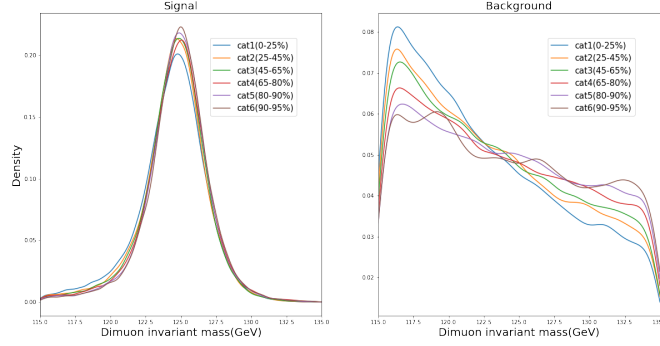
oretically well-motivated training variables such as p_T, η and so on. It is also easy to interpret the result. However, compared to network-based models, it lacks the ability of capturing complex non-linear relationships among training variables. Generally it is the reason why network based discriminators such DNN are preferred for more complex data. Ironically, this intrinsic weakness of tree-based model would be profitable for making the resultant discriminator to be independent to $m_{\mu\mu}$.

To compare our result, we also conducted the BDT discrimination. We used the

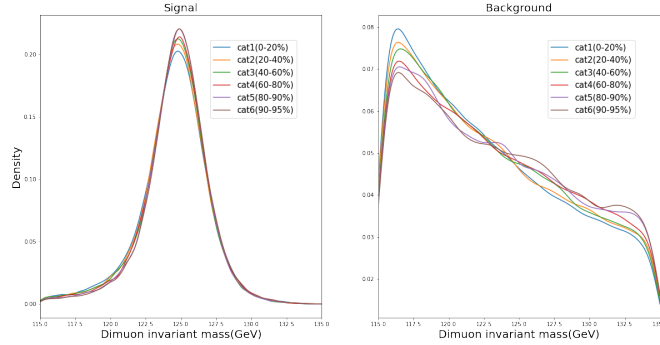
gradient-boosted tree implemented in **SCIKIT LEARN**. The Friedman MSE is used as a splitting criterion and a deviance is used as a loss. Selected models are given in Appendix.B 1. Fig.2 shows $m_{\mu\mu}$ distribution categorized by output of BDT discriminators. It is obvious that the $m_{\mu\mu}$ distributions are much more similar compared to the ordinary DNN case(Fig.1). However, the distributions are not exactly the same. There is a difference in slope of background distributions which also can be problematic for extracting the number of signal events. Actually the CMS collaboration was aware of it and use mass side band events to constrain the background distribution with modified fitting function having common shape and category specific slope (The ‘core-pdf’ method).

For both BDT and DNN, the discrimination result is not statistically independent to $m_{\mu\mu}$. To achieve the independence, we exploit the flexibility of DNN. The network in DNN is an analytic function and it can handle wide variety of loss functions, which only requires to be differentiable. Therefore we included ‘decorrelation loss’ $\mathcal{L}_{\text{decor}}$ with a parameter λ as $\mathcal{L}_{\text{tot}} \equiv \mathcal{L}_{\text{discrim}} + \lambda\mathcal{L}_{\text{decor}}$, where the discrimination loss $\mathcal{L}_{\text{discrim}}$ is the binary cross entropy. The $\mathcal{L}_{\text{discrim}}$ and $\mathcal{L}_{\text{decor}}$ are in conflict since $m_{\mu\mu}$ has strong discrimination power. However what we want to achieve is the decorrelation even if it costs discrimination performance. It can be achieved by setting λ to be large enough. The distance correlation ($\equiv \mathcal{R}$) is used as a measure of statistical dependence. We required the discrimination score to be independent to $m_{\mu\mu}$ separately for signal and background events, $\mathcal{L}_{\text{decor}} \equiv \mathcal{R}(m_{\mu\mu}, \text{score}|\text{signal}) + \mathcal{R}(m_{\mu\mu}, \text{score}|\text{background})$. We will call this DNN model with decorrelation loss as ‘decorrelated DNN’.

The decorrelated DNN is implemented with **PyTorch** again. We added decorrelation loss term every two epochs for calculation efficiency. Furthermore, since the distance matrix requires large memory, 1% of every batch is sampled to calculate \mathcal{R} . To test the degree of decorrelation at the end of training, the distance correlation is calculated with sample of size 25,000 for signal and background respectively (which is actually



(a) BDT; **without** jet substructure variables($S_{n_{jet}}$)



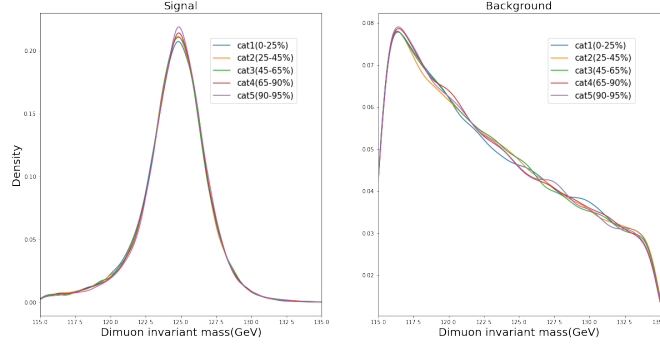
(b) BDT; **with** jet substructure variables(S_0, J_1 and J_2)

FIG. 2. $m_{\mu\mu}$ distribution binned by optimal boundaries chosen by output of BDT discriminators.

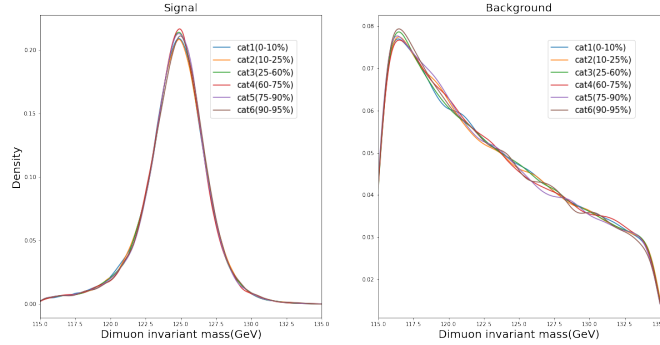
the limitation of our gpu memory). Selected models are given in Appendix.B 3. Fig.3 shows the $m_{\mu\mu}$ distributions which are not distorted by the categorization. Therefore, there will be no systematic error from dependence.

A. Comparison

As mentioned before, the decorrelation is in conflict with discrimination. Therefore the comparison among three machine discriminators - BDT, (ordinary)DNN and



(a) decorrelated DNN; **without** jet substructure variables ($S_{n_{\text{jet}}}$)



(b) decorrelated DNN; **with** jet substructure variables ($J_{n_{\text{jet}}}$)

FIG. 3. $m_{\mu\mu}$ distribution binned by optimal boundaries chosen by output of decorrelated DNN discriminators.

decorrelated DNN - can be summarized in terms of two properties, the performance of discrimination and the degree of decorrelation. Fig. 4 shows the receiver operating characteristic (ROC) curve with area under curve (AUC). It shows the performance of each discriminator. For all three discriminators, including jet substructure variables (solid lines) improve the discrimination performance of ggH channel. The ordinary DNN's (black) have large AUC since they exploited $m_{\mu\mu}$ internally. BDT (blue) and decorrelated DNN (red) have similar AUCs, which is around 0.1 less than those of

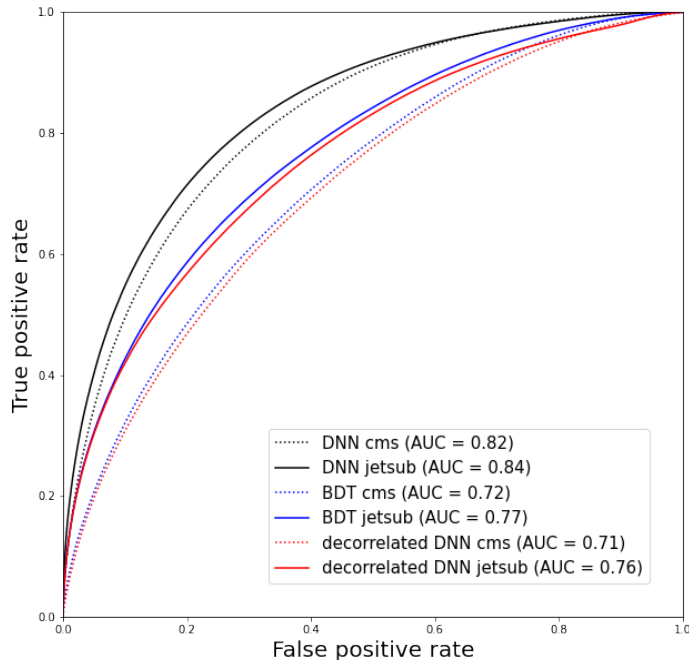


FIG. 4. Receiver operating characteristic(ROC) curve for three discrimination schemes - BDT, (ordinary) DNN and decorrelated DNN - with two different set of variables($S_{n_{\text{jet}}}$ and $JS_{n_{\text{jet}}}$). The area under curve(AUC) is also given. Note that the true positive rate is equivalent to signal efficiency and the false positive rate is equivalent to (1-background rejection rate).

ordinary DNN. The gap between ordinary DNN's and other methods represents the discrimination power of $m_{\mu\mu}$, or more conservatively, power of the information of training variables correlated to $m_{\mu\mu}$. The small AUC's of decorrelated DNN reflects that the decorrelation intentionally discards the information about $m_{\mu\mu}$ and those of BDT reflects that the BDT cannot reconstruct $m_{\mu\mu}$ internally. The small difference of AUC between BDT and decorrelated can be interpreted as the the uncontrolled contamination by $m_{\mu\mu}$.

The degree of decorrelation between $m_{\mu\mu}$ and the output of discriminators can be seen directly from the distortion of invariant mass distribution categorized by the output of discriminators (Fig.1, 2, 3). It can also be quantitatively checked by a test of independence using asymptotic distribution of distance covariance \mathcal{V} [11]. The test statistic is $V \equiv \frac{n \times \mathcal{V}^2(X, Y)}{S_2}$, where n is the size of sample and $S_2 \equiv \frac{1}{n^2} \sum_{k, l} |X_k - X_l| \frac{1}{n^2} \sum_{k, l} |Y_k - Y_l|$. The statistical independence would be rejected if $\sqrt{V} > \Phi^{-1}(1 - \alpha/2)$ for selected significance level α , where Φ is the Gaussian cumulative density function.

Fig.5 shows the statistic \sqrt{V} between $m_{\mu\mu}$ and the output of discriminator. Samples of size 10000 with 1000 iterations are used. It is interesting that the result becomes more independent for all the cases when the jet substructure variables are included for training. This is because jet substructure variables are useful for discrimination of ggH signal from background but relatively less correlated to $m_{\mu\mu}$ compared to $S_{n_{\text{jet}}}$ variables including information about muon and dimuon system. It is obvious that $m_{\mu\mu}$ and the output of discriminators are enormously correlated for (ordinary) DNN. The independence hypothesis is always rejected for DNN case even under $\alpha < 0.05$. The situation is improved in the case of BDT but the uncontrolled impact of $m_{\mu\mu}$ still exist. The BDT trained with jet substructure variables barely pass the test up to $\alpha = 0.05$. On the other hand, the output of decorrelated DNN and $m_{\mu\mu}$ is independent up to $\alpha = 0.215$, which is the upper limit of significance level given in [11].

B. Decorrelated DNN result in detail

After imposing distance correlation loss, the decorrelated DNN loses its accuracy but becomes independent of $m_{\mu\mu}$. Therefore the $m_{\mu\mu}$ can be used without systematic error after categorization. Now, have a detailed look at the categorization result of

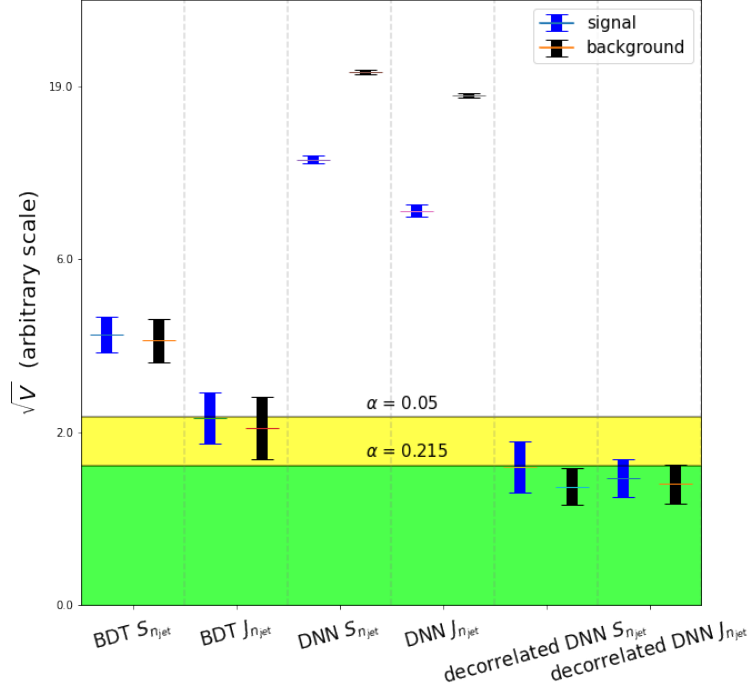
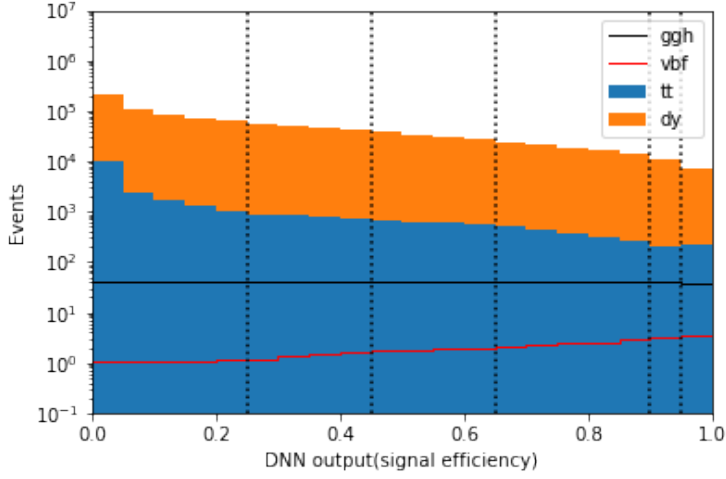


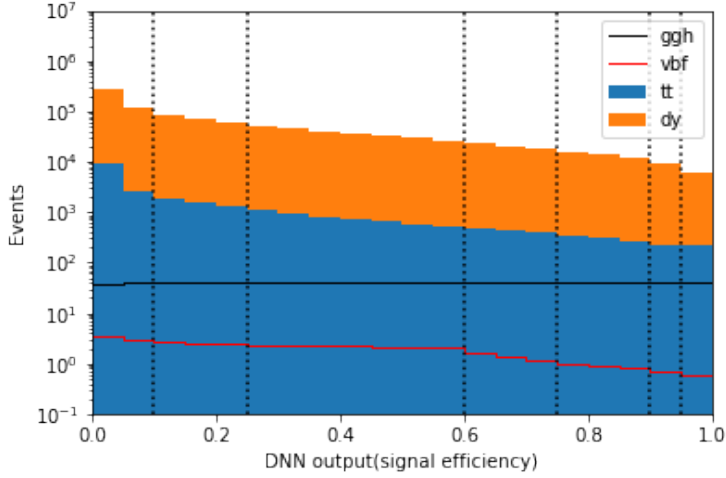
FIG. 5. The statistic \sqrt{V} of signal and background separately for various discriminators. The error bar comes from 1,000 iterations and sample size 10,000 was used. Please note that the scale of y-axis is arbitrary.

decorrelated DNN.

Fig.6 shows the number of events for each category and production channel. The number of signal and background is stacked respectively. The vertical dotted lines are the optimal boundaries. Table.I, II shows the number of signal, portion of each production channel, number of background, $S/(S + B)$ and S/\sqrt{B} for optimized categories without and with jet substructure variables. In Fig.6a and Table.I, the portion of VBF among signal is larger for higher purity category. This tendency stems from the discrimination power of two characteristic jets of VBF. On the other



(a) **without** jet substructure variables ($S_{n_{jet}}$)



(b) **with** jet substructure variables ($J_{n_{jet}}$)

FIG. 6. Number of events according to optimized bins according to signal efficiency. (a)/(b): For a model trained **without/with** jet substructure variables.

hand, the tendency of growing VBF portion is totally reversed for the discriminators trained with jet substructure variables. In Fig.6b, Table.II, the portion of VBF

events are getting smaller for higher signal purity category. This reversal of VBF portion represents the improved discrimination power of ggH signals by exploiting jet substructure variables. This property can be used to reduce errors from analysis done separately for each production channel and improve the precision of ggH channel.

| Signal efficiency | Sig | ggH (%) | VBF (%) | Bkg | $\frac{S}{S+B}$ (%) | $\frac{S}{\sqrt{B}}$ |
|-------------------|--------|---------|---------|--------|---------------------|----------------------|
| 0-25% | 212.45 | 97.5 | 2.5 | 545713 | 0.04 | 0.29 |
| 25-45% | 169.93 | 96.6 | 3.4 | 193690 | 0.09 | 0.39 |
| 45-75% | 170.17 | 95.6 | 4.4 | 130068 | 0.13 | 0.47 |
| 75-90% | 212.65 | 94.2 | 5.8 | 96033 | 0.22 | 0.69 |
| 90-95% | 42.65 | 92.5 | 7.5 | 11317 | 0.38 | 0.40 |
| 95-100% | 42.41 | 91.3 | 8.6 | 7254 | 0.58 | 0.50 |

TABLE I. Categorization for decorrelated DNN **without** jet substructure variables.

| Signal efficiency | Sig | ggH (%) | VBF (%) | Bkg | $\frac{S}{S+B}$ (%) | $\frac{S}{\sqrt{B}}$ |
|-------------------|--------|---------|---------|--------|---------------------|----------------------|
| 0-10% | 85.09 | 92.6 | 7.4 | 389125 | 0.02 | 0.14 |
| 10-25% | 127.42 | 94.0 | 6.0 | 216714 | 0.06 | 0.27 |
| 25-60% | 297.62 | 94.7 | 5.3 | 260441 | 0.11 | 0.58 |
| 60-75% | 127.66 | 96.7 | 3.3 | 61487 | 0.21 | 0.51 |
| 75-90% | 127.53 | 97.9 | 2.1 | 40971 | 0.31 | 0.63 |
| 90-95% | 42.52 | 98.3 | 1.7 | 9348 | 0.45 | 0.44 |
| 95-100% | 42.41 | 98.6 | 1.4 | 5933 | 0.71 | 0.55 |

TABLE II. Categorization for decorrelated DNN **with** jet substructure variables.

IV. DISCOVERY SIGNIFICANCE

The statistical significance is calculated by the profile likelihood ratio fit to the $m_{\mu\mu}$. We used uniform binning of size 50 MeV. To incorporate systematic errors, nuisance parameters θ are included with Gaussian suppression. Since the simulation was done for arbitrary luminosity, the number of events are normalized to that of [7], 137 fb^{-1} .

We used non-integers from the normalization directly to Poisson counts to avoid the subtle risk of getting the over- or under-estimated results from the rounding off. The problem of non-integers for Poisson distribution is not a genuine problem since it will be canceled off by calculating likelihood ratio [17].

To compare the result, significance is computed for BDT and decorrelated DNN. We do not compute for ordinary DNN case since it is totally distorted. Please note that since we do not extract the number of events by fitting and use the simulation data directly, the significance computed for BDT do not suffer from the problem in extraction though there is distortion indeed. The true significance will be different but cannot predict the tendency since it largely depend on the prescriptions such as the ‘core-pdf’ method used in [7]. Table.III shows the AUC and significance. Clearly, significance increases about 0.15 by exploiting ggH ISR characteristic. The slightly difference of AUC and significance between BDT and decorrelated dNN can be interpreted as uncontrolled impact of $m_{\mu\mu}$.

| Machine Variables | BDT | | decorrelated DNN | |
|----------------------|----------------------|----------------------|----------------------|----------------------|
| | $S_{n_{\text{jet}}}$ | $J_{n_{\text{jet}}}$ | $S_{n_{\text{jet}}}$ | $J_{n_{\text{jet}}}$ |
| significance | (1.64) | (1.78) | 1.61 | 1.76 |
| AUC | 0.72 | 0.77 | 0.71 | 0.76 |

TABLE III. Discovery significance table. CMS benchmark was 1.56σ for ggH and 1.77σ for VBF. The numbers in the parenthesis are obtained without sufficient decorrelation and should be interpreted cautiously.

V. SUMMARY

We applied decorrelation using distance correlation to the Higgs to dimuon discovery from ggH channel. The decorrelation between output of discriminator and $m_{\mu\mu}$ allows us to categorize the events without any systematic error from $m_{\mu\mu}$ correlations. The

decorrelated DNN achieved the independence simultaneously for both signal and background events up to significance level $\alpha = 0.215$. The jet substructure variables are helpful for improving discovery significance of ggH channel and the significance was improved from 1.61 to 1.76.

Decorrelation can be helpful in general for both precision and discovery researches as it can preserve the variable of interest-distribution of events after the cut and get rid of systematic errors from distortion in the process of categorization. In addition, all the variables can be used for categorization without any concern of correlation.

VI. ACKNOWLEDGEMENTS

We thank Wonsang Cho for collaboration at an initial stage of the work and for discussion and comments. This work is supported by NRF of Korea grant, No. 0426-20230001.

Appendix A: Training variables

The set of training variables for events with each number of jets n_{jet} will be summarized. We will denote the variables used by the CMS collaboration without jet substructure variables as $S_{n_{\text{jet}}}$ and variables with jet substructure variables as $J_{n_{\text{jet}}}$. Please note that $n_{\text{jet}} = 2$ means events with at least two jets. Therefore S_2 and J_2 mean training variables for events with multi-jets, not only events with exactly two jets.

1. CMS used variables

The training variables were carefully selected to exclude $m_{\mu\mu}$ information. The set of training variables $S_{n_{\text{jet}}}$ used by CMS collaboration are

$$\begin{aligned}
 S_0 &\equiv \{p_T^{\mu\mu}, y_{\mu\mu}, \phi_{CS}, \cos \theta_{CS}, \eta(\mu_1), \eta(\mu_2) \\
 &\quad, \frac{p_T^{\mu 1}}{m_{\mu\mu}}, \frac{p_T^{\mu 2}}{m_{\mu\mu}}\} \\
 S_1 &\equiv S_0 \cup \{p_T(j_1), \eta(j_1), \Delta R(\mu\mu, j_1)\} \\
 S_2 &\equiv S_1 \cup \{p_T(j_2), \eta(j_2), m_{j_1 j_2}, \Delta \eta_{j_1 j_2}, \Delta \phi_{j_1 j_2} \\
 &\quad, \Delta \eta_{\mu\mu, j_1}, \Delta \eta_{\mu\mu, j_2}, \Delta \phi_{\mu\mu, j_1}, \Delta \phi_{\mu\mu, j_2} \\
 &\quad, z_*, n\}
 \end{aligned}$$

In the above notation, CS means those computed in the dimuon Collins-Soper rest frame, $j_{1,2}$ respectively denotes the highest and second highest p_T jet, $z_* \equiv \frac{y_{\mu\mu} - (y_{j_1} + y_{j_2})/2}{|y_{j_1} - y_{j_2}|}$ is the Zeppenfeld variable and n is the number of jets with $p_T > 25\text{GeV}$, $|\eta| < 4.7$.

2. Jet substructure variables

To exploit the ISR characteristic of ggH channel, we used jet substructure variables in addition to the conventional variables. The jet substructure variables are generally defined as weighted moment sum of constituent transverse momenta normalized by transverse momentum of the jet to capture the fatness of gluon jet. For each jet, we used the number of charged tracks in the jet n_{track} [18], girth (linear radial moment) [18][19], broadening[20], Energy-energy correlation(EEC) $C_1^{\beta=0.2}$ with $\beta = 0.2$

[21][22], RMS- p_T [18], Pull-vector[23].

$$\begin{aligned}
\text{girth } G &= \frac{1}{p_T^{\text{jet}}} \sum_{i \in \text{jet}} p_T^i |\Delta \vec{r}_i| \\
\text{broadening } B &= \frac{1}{\sum_i |\vec{p}^i|} \sum |\vec{p}^i \times \hat{p}^{\text{jet}}| \\
&= \frac{1}{\sum_i |\vec{p}^i|} \sum |\vec{k}_T^i| \\
\text{EEC } C_1^\beta &= \frac{1}{(\sum_i p_T^i)^2} \sum_{i < j} p_T^i p_T^j (\Delta R_{ij})^\beta \\
\text{RMS-}p_T \sqrt{\langle p_T^2 \rangle} &= \frac{1}{p_T^{\text{jet}}} \sqrt{\frac{1}{n_{\text{tk}}} \sum_i (p_T^i)^2} \\
\text{Pull-vector } \vec{v}_p &= \frac{1}{p_T^{\text{jet}}} \sum_i p_T^i |\Delta \vec{r}^i| \Delta \vec{r}^i
\end{aligned}$$

Appendix B: Discrimination models in detail

1. BDT

A minimum sample size for a node to be split (`min_samples_split`) is 1% to regularize the over-fitting. We used stochastic gradient boosting with 70% of sample for each tree. Table IV shows the resultant (hyper-)parameters and accuracy for each machine. The minimum sample size after the splitting is once more limited by `min_samples_leaf` (MSL).

2. (Ordinary) DNN

Table V shows the resultant (hyper-)parameters and accuracy for each ordinary DNN machine. Through all the machines, 256 nodes per layer and 100 batches are commonly used.

| Variables | w/o jet sub. | | | w/ jet sub. | |
|-------------------|--------------|-------|-------|-------------|-------|
| | S_0 | S_1 | S_2 | J_1 | J_2 |
| n_{tree} | 80 | 1500 | 1000 | 1500 | 1000 |
| max depth | 3 | 5 | 7 | 7 | 9 |
| learning rate | 0.4 | 0.2 | 0.2 | 0.1 | 0.1 |
| MSL | 0.001 | 0.01 | 0.02 | 0.001 | 0.001 |
| accuracy | 0.66 | 0.65 | 0.66 | 0.72 | 0.73 |

TABLE IV. (hyper-)Parameters and accuracy of BDT. MSL stands for min_samples_leaf.

| Variables | w/o jet sub. | | | w/ jet sub. | |
|---------------------------|--------------|-------|-------|-------------|-------|
| | S_0 | S_1 | S_2 | J_1 | J_2 |
| n_{layers} | 2 | | | 3 | |
| learning rate | 0.007 | 0.01 | 0.003 | 0.04 | 0.005 |
| epochs | 100 | 300 | 400 | 300 | 300 |
| accuracy | 0.76 | 0.75 | 0.75 | 0.79 | 0.79 |
| $\mathcal{R}(\text{sig})$ | 0.35 | 0.39 | 0.33 | 0.32 | 0.24 |
| $\mathcal{R}(\text{bkg})$ | 0.31 | 0.31 | 0.30 | 0.28 | 0.18 |

TABLE V. (hyper-)Parameters and accuracy of DNN. The resultant distance correlation \mathcal{R} the distance correlation \mathcal{R} is calculated with 25,000 events each from the test sample.

3. Decorrelated DNN

Table VI shows the resultant (hyper-)parameters and accuracy for each decorrelated DNN machine. Through all the machines, 128 nodes per layers and 100 batches are commonly used. The relative multiplier $\lambda = 8 \times 10^{-3}$ is also common. We made the λ to be magnified to 100 times of its input value if $\mathcal{L}_{\text{decor}} > 10^{-3}$ during the training. Therefore the $\lambda = 8 \times 10^{-1}$ for almost all the time during the training. Since the $\mathcal{L}_{\text{decor}}$ is the sum of distance correlations of signal and background and it is computed with smaller sample, it is larger than the value of distance correlation computed for the test sample(**).

| Variables | w/o jet sub. | | | w/ jet sub. | |
|--------------------------------|--------------|-------|-------|-------------|-------|
| | S_0 | S_1 | S_2 | J_1 | J_2 |
| n_{layers} | 3 | 3 | 6 | 3 | 6 |
| learning rate | 0.0004 | 0.001 | 0.01 | 0.001 | 0.001 |
| epochs | 30 | 40 | 60 | 60 | 60 |
| $\mathcal{L}_{\text{decor}}^*$ | 0.046 | 0.047 | 0.044 | 0.037 | 0.038 |
| accuracy | 0.65 | 0.64 | 0.65 | 0.71 | 0.72 |
| $\mathcal{R}(\text{sig})^{**}$ | 0.006 | 0.009 | 0.011 | 0.008 | 0.008 |
| $\mathcal{R}(\text{bkg})^{**}$ | 0.019 | 0.018 | 0.022 | 0.010 | 0.010 |

TABLE VI. Resultant model (hyper-)parameters and accuracy. *: $\mathcal{L}_{\text{decor}}$ is the sum of distance correlation loss between score and $m_{\mu\mu}$ respectively for signal and background. 1% of every batch is sampled to calculate $\mathcal{L}_{\text{decor}}$. **: Here the distance correlation \mathcal{R} is calculated with 25,000 events each from the test sample.

Appendix C: Independence test

We checked the performance of test using V with the well-known distribution, the two-dimensional Gaussian with various correlation. Fig.7 shows the fraction of rejected samples among 500 iterations (equivalent to type 1 error rate for zero correlation case and statistical power for non-zero correlation cases) with different sample size and correlation. More than sample size 5000, the samples with correlation ≥ 0.1 are all rejected for significance level $\alpha \geq 0.1$.³ Thus we conducted the test of independence with size 5000 and significance level $\alpha = 0.215$ for 500 iterations. The rejected fraction is given in Table.VII

| Machine | BDT | | DNN | | decor.DNN | |
|----------|----------------------|----------------------|----------------------|----------------------|----------------------|----------------------|
| Variable | $S_{n_{\text{jet}}}$ | $J_{n_{\text{jet}}}$ | $S_{n_{\text{jet}}}$ | $J_{n_{\text{jet}}}$ | $S_{n_{\text{jet}}}$ | $J_{n_{\text{jet}}}$ |
| sig(%) | 100 | 76.6 | 100 | 100 | 30.2 | 17.4 |
| bkg(%) | 99.8 | 64.6 | 100 | 100 | 12.0 | 16 |

TABLE VII. Rejection rate among 500 iterations for the test of dependence. Significance level $\alpha = 0.215$ and size = 5000 was used.

³ In Table 1 of [11], they reported type 1 error rate about 0.1 for various independent distributions, sample sizes under $\alpha = 0.1$. In Fig. 2, the power of test for Gaussian with correlation $\rho = 0.1$ and under $\alpha = 0.1$ is also given.

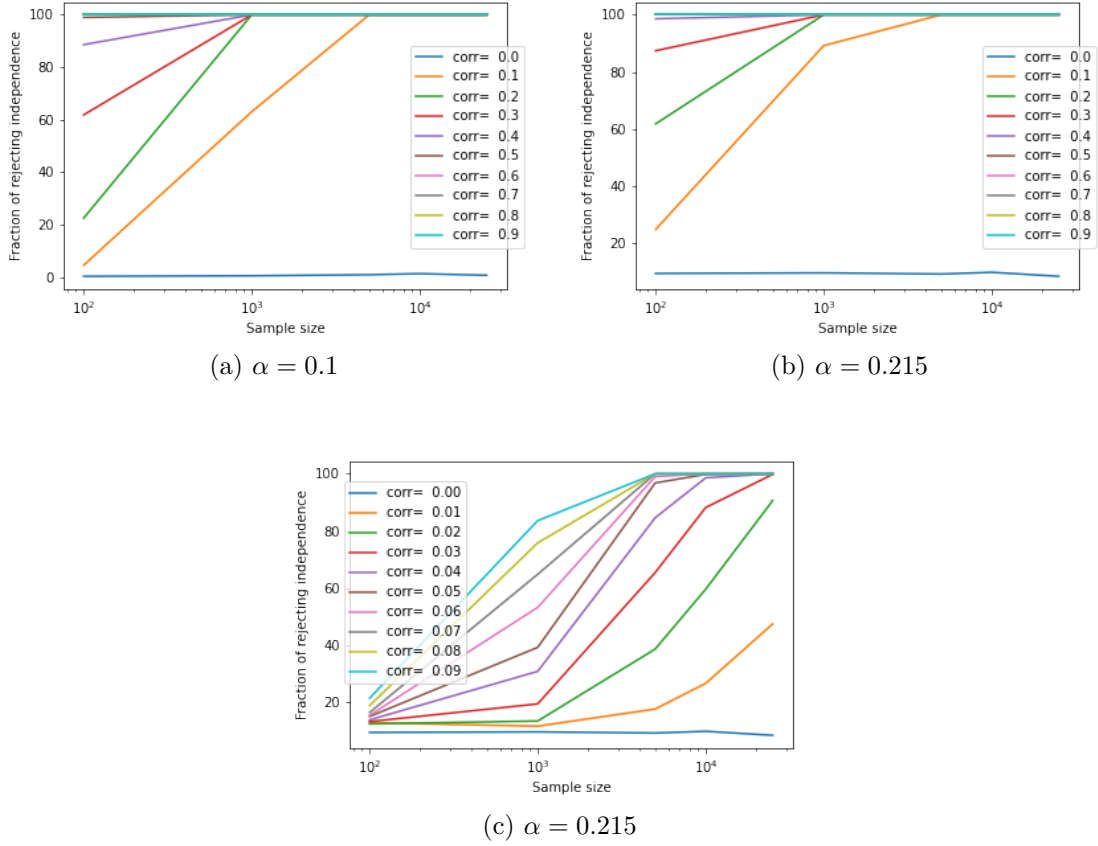


FIG. 7. Fraction of rejected samples among 500 iterations with two-dimensional Gaussian, for various sample size, correlation and significance level α

-
- [1] S. Chatrchyan et al. (CMS Collaboration), Physics Letters B **716**, 30 (2012).
 - [2] G. Aad et al. (ATLAS Collaboration), Physics Letters B **716**, 1 (2012).
 - [3] G. Aad et al. (ATLAS Collaboration), Phys. Rev. D **101**, 012002 (2020).
 - [4] Aaboud et al. (ATLAS Collaboration), Physics Letters B **784**, 173 (2018).
 - [5] Sirunyan et al. (CMS Collaboration), Physical review letters **121**, 121801 (2018).

- [6] Aaboud et al. (ATLAS Collaboration), Physical Review D **99**, 072001 (2019).
- [7] A. M. Sirunyan et al. (CMS Collaboration), JHEP **01**, 148 (2021), arXiv:2009.04363 [hep-ex].
- [8] N. Altman and M. Krzywinski, Nature Methods **12**, 899 (2015).
- [9] G. Kasieczka and D. Shih, Physical Review Letters **125** (2020), 10.1103/physrevlett.125.122001.
- [10] D. Bourilkov, D. Acosta, P. Bortignon, A. Brinkerhoff, A. Carnes, S. Gleyzer, and B. Regnery (CMS Collaboration), EPJ Web Conf. **214**, 06002 (2019).
- [11] G. J. Székely, M. L. Rizzo, and N. K. Bakirov, The Annals of Statistics **35** (2007), 10.1214/009053607000000505.
- [12] CERN, “Cern yellow reports: Monographs, vol 2 (2017): Handbook of lhc higgs cross sections: 4. deciphering the nature of the higgs sector,” (2017).
- [13] W. S. Cho, H. D. Kim, and D. Lee, Physical Review D **102** (2020), 10.1103/physrevd.102.115007.
- [14] J. Alwall, R. Frederix, S. Frixione, V. Hirschi, F. Maltoni, O. Mattelaer, H. S. Shao, T. Stelzer, P. Torrielli, and M. Zaro, JHEP **07**, 079 (2014), arXiv:1405.0301 [hep-ph].
- [15] A. Paszke, S. Gross, F. Massa, A. Lerer, J. Bradbury, G. Chanan, T. Killeen, Z. Lin, N. Gimelshein, L. Antiga, et al., “Pytorch: An imperative style, high-performance deep learning library,” (2019), arXiv:1912.01703 [cs.LG].
- [16] F. Pedregosa, G. Varoquaux, A. Gramfort, V. Michel, B. Thirion, O. Grisel, M. Blondel, P. Prettenhofer, R. Weiss, V. Dubourg, et al., the Journal of machine Learning research **12**, 2825 (2011).
- [17] G. Cowan, K. Cranmer, E. Gross, and O. Vitells, The European Physical Journal C **71**, 1 (2011).
- [18] J. Gallicchio and M. D. Schwartz, Physical Review Letters **107** (2011), 10.1103/physrevlett.107.172001.

- [19] J. Gallicchio, J. Huth, M. Kagan, M. D. Schwartz, K. Black, and B. Tweedie, *Journal of High Energy Physics* **2011**, 1 (2011).
- [20] S. Catani, G. Turnock, and B. R. Webber, *Phys. Lett. B* **295**, 269 (1992).
- [21] A. J. Larkoski, G. P. Salam, and J. Thaler, *Journal of High Energy Physics* **2013** (2013), 10.1007/jhep06(2013)108.
- [22] M. Dasgupta, A. Fregoso, S. Marzani, and G. P. Salam, *Journal of High Energy Physics* **2013** (2013), 10.1007/jhep09(2013)029.
- [23] J. Gallicchio and M. D. Schwartz, *Phys. Rev. Lett.* **105**, 022001 (2010), arXiv:1001.5027 [hep-ph].